LAWRENCE
LIVERMORE
NATIONAL
LABORATORY

UCRL-TR-234682

Microscopic Calculations of 240Pu Fission

W. Younes, D. Gogny

September 18, 2007

This work was performed under the auspices of the U.S. Department of Energy by University of California, Lawrence Livermore National Laboratory under Contract W-7405-Eng-48.

Microscopic calculations of ^{240}Pu fission

W. Younes and D. Gogny

Lawrence Livermore National Laboratory, Livermore, CA 94551

(Dated: 11th September 2007)

Abstract

Hartree-Fock-Bogoliubov calculations have been performed with the Gogny finite-range effective interaction for ^{240}Pu out to scission, using a new code developed at LLNL. A first set of calculations was performed with constrained quadrupole moment along the path of most probable fission, assuming axial symmetry but allowing for the spontaneous breaking of reflection symmetry of the nucleus. At a quadrupole moment of 345 b, the nucleus was found to spontaneously scission into two fragments. A second set of calculations, with all nuclear moments up to hexadecapole constrained, was performed to approach the scission configuration in a controlled manner. Calculated energies, moments, and representative plots of the total nuclear density are shown. The present calculations serve as a proof-of-principle, a blueprint, and starting-point solutions for a planned series of more comprehensive calculations to map out a large set of scission configurations, and the associated fission-fragment properties.

I. INTRODUCTION

The quantitative description of fission is arguably the most daunting challenge in nuclear physics. Since the official discovery of fission in 1939 [1], a predictive theory of this phenomenon has remained elusive. However, recent developments in the formalism, coupled with the advent of parallel programming, have made the microscopic treatment of fission within the framework of quantum many-body theory feasible. The microscopic approach to fission, embodied in the Hartree-Fock (HF) method, and augmented by a set of extensions beyond the mean-field approximation (e.g., the Bogoliubov formalism used to include pairing correlations, the random-phase approximation used to include residual particle-hole correlations, etc.), is the only formalism that is potentially capable of producing the long-sought-after predictive theory of this phenomenon.

A program to develop a microscopic theory of fission has been started at LLNL. The program is based on the highly successful work [2–4] at the Bruyères-le-Châtel nuclear-physics laboratory. To this end, the Hartree-Fock code FRANCHFRI [5] (Finite-RANge Constrained Hartree-Fock Rapid Iterator) was written using a finite-range effective interaction developed by D. Gogny [6]. The critical importance of a finite-range effective interaction in Hartree-Fock calculations, compared to the zero-range Skyrme interaction more commonly used, has already been emphasized [5, 7]. With the zero-range interaction, the mathematical pathologies of the delta function make it impossible to treat the particle-hole and particle-particle (i.e., pairing) interactions on the same footing, thereby violating the strict meaning of self-consistency in the theory, which is the crux of the microscopic approach. The finite-range effective interaction does not suffer from such pathologies and, therefore, is essential for a truly self-consistent approach to the fission problem.

The code FRANCHFRI has now been extended to include pairing correlations, and multiple constraints. This new code, FRANCHBRIE (Finite-RANge Constrained Hartree-Fock-Bogoliubov with Rapid Iteration Execution), will be discussed in detail in a forthcoming report. Pairing is introduced in the code within the framework of the Hartree-Fock-Bogoliubov (HFB) formalism [8]. Multiple constraints are treated by the method of Lagrange multipliers, expressed in a matrix formalism to take into account correlations between the various constraints. Six constraints have been programmed into the current version of the code, and they are those required for a meaningful treatment of fission: the average number of neu-

trons ($\langle N_n \rangle$), the average number of protons ($\langle N_p \rangle$), the dipole moment ($\langle Q_{10} \rangle$, used to keep the center of mass of the nucleus fixed when reflection symmetry is broken), the quadrupole moment ($\langle Q_{20} \rangle$, used to control the elongation of the nucleus), the octupole moment ($\langle Q_{30} \rangle$, used to produce a left-right asymmetry), and the hexadecapole moment ($\langle Q_{40} \rangle$, used to control the thickness of the neck separating the two fragments when the nucleus is about to scission).

The constrained HFB code can be used to calculate the state of the nucleus at scission. Fig. 3 of ref. [3] shows an energy surface (labeled N1) formed by a set of HFB calculations for ^{240}Pu, constrained in $\langle Q_{20} \rangle$ and $\langle Q_{30} \rangle$. On the surface N1, the nucleus remains whole, however, for any given octupole moment $\langle Q_{30} \rangle$, there is always a quadrupole moment $\langle Q_{20} \rangle$ large enough for a new solution to develop, corresponding to two well-separated fragments. This solution is represented by the surface N2 in the figure. When the surface N2 crosses below N1, the separated configuration for the nucleus becomes energetically favorable. The surfaces N1 and N2 can be seen in a more consistent picture in Fig. 4 of [3]. The figure shows the energy surface corresponding to HFB solutions for ^{240}Pu, constrained in $\langle Q_{20} \rangle$ and $\langle Q_{40} \rangle$ this time, for a particular mass split of the nucleus (i.e., for a particular set of values of the constraints in$\langle Q_{20} \rangle$ and $\langle Q_{30} \rangle$). In the figure, two valleys are visible, labeled V1 and V2, and corresponding to the surfaces N1 and N2, respectively, in Fig. 3 of [3]. A ridge separates the valleys V1 and V2 but, as $\langle Q_{20} \rangle$ increases, that ridge can be seen to diminish and eventually disappear near $\langle Q_{20} \rangle = 350$ b. At that value of the quadrupole moment, a nucleus in V1 spontaneously drops into valley V2 and breaks apart. The drop in energy from V1 to V2 at $\langle Q_{20} \rangle = 350$ b is large, on the order of 30 MeV. Scission at $\langle Q_{20} \rangle = 350$ b therefore corresponds to the so-called "hot" fission, where the fragments are formed with a great deal of excitation energy. However, it is possible for the nucleus to exit V1 and drop into V2 at any value of $\langle Q_{20} \rangle$ before 350 b in Fig. 4 of [3]. If this exit occurs at 250 b, for example, the drop in energy is much lower, about 10 MeV, corresponding to "cold" fission. Thus, the constrained-HFB method contains the full rich range of phenomena expected in the fission process.

The immediate goal of the LLNL microscopic fission program is to calculate the properties of the fission fragments at scission, e.g., their excitation energies, their kinetic energies, their shapes, etc., before the fragments have de-excited to their respective ground states. From these initial properties, the subsequent neutron and gamma emission spectra can be deduced.

To this end, it is essential to constrain the HFB solution so that the nucleus does not drop into valley V2 of Fig. 4 in [3]. If the HFB solution reaches the bottom of V2, the fragments will be de-excited to their ground state by the variational procedure, and all useful information about their state at scission will be lost. In this report, we present calculations out to scission for the most probable path to scission. This is the path that follows the bottom of the valley in Fig. 3 of [3], and exits valley V1 in Fig. 4 of [3] at the "hot" scission point near $\langle Q_{20} \rangle = 350$ b. This result serves as both a proof-of-principle for the proposed approach to map out the scission configurations for a large set of values of $(\langle Q_{20} \rangle, \langle Q_{30} \rangle, \langle Q_{40} \rangle)$, and an exposition of the necessary tools and techniques. The approach can then be repeated for all other exit points $(\langle Q_{20} \rangle, \langle Q_{30} \rangle, \langle Q_{40} \rangle)$.

II. METHOD

The calculations for ^{240}Pu presented in this report were carried out in two phases. First, a constraint was placed on $\langle Q_{20} \rangle$ (as well as the average neutron and proton numbers, as required by the HFB formalism). At the larger deformations ($\langle Q_{20} \rangle \geq 100$ b), where the reflection symmetry of the nucleus can be spontaneously broken, a constraint was also placed on the dipole moment to force $\langle Q_{10} \rangle = 0$, and thereby guarantee that the center of mass of the nucleus remained fixed. The remaining moments (namely $\langle Q_{30} \rangle$ and $\langle Q_{40} \rangle$) were left free, and the variational HFB procedure yielded those values of $\langle Q_{30} \rangle$ and $\langle Q_{40} \rangle$ that minimize the energy of the nucleus. These calculations were performed from $\langle Q_{20} \rangle = 0$ to 345 b, and it was found that, beginning at $\langle Q_{20} \rangle = 350$ b, the nucleus spontaneously split into two fragments, and the overall energy began to drop, corresponding to the de-excitation of the individual fragments. In a second phase, the scission limit was approached in incremental steps by constraining $\langle Q_{20} \rangle$ to 345 b, and $\langle Q_{30} \rangle$ to have the value reached for $\langle Q_{20} \rangle = 345$ b in the first phase of the calculation, namely $\langle Q_{30} \rangle = 46$ b$^{3/2}$. The hexadecapole moment was also constrained to its final value at $\langle Q_{20} \rangle = 345$ b, namely 190 b^2, and then stepped down by decrements of 1 b^2 in subsequent calculations. This procedure required calculations with all six constraints available in the current version of FRANCHBRIE. This approach is well-suited for a microscopic calculation of "hot" fission along the most likely path to scission. In the first phase of the calculations described above, the nucleus is driven to the point where its deformation is so large that it fission spontaneously and, in the second phase, a

constraint on the thickness of the neck (via the hexadecapole moment) is introduced to hold the nucleus back from the brink and to approach the scission configuration in a controlled manner.

The current version of the code assumes axial symmetry, and works in the deformed cylindrical harmonic-oscillator basis, characterized by four quantum numbers: the number of nodes in the radial direction ($n_\perp \geq 0$), the projection of the orbital angular momentum on the symmetry axis (Λ), the number of nodes in the z direction ($n_z \geq 0$), and the projection of the intrinsic spin on the symmetry axis ($\sigma = \pm 1/2$). The basis size is controlled through the choice of two parameters. The first parameter is an integer, the largest shell number N included in the calculation, which provides the constraint

$$0 \ \leq 2n_\perp + |\Lambda| \leq \ N$$

The second parameter controlling the basis size is the real number q, with $q > 0$, and such that

$$0 \ \leq 2n_\perp + |\Lambda| + \tfrac{n_z}{q} \leq \ N$$

Thus by choosing $q > 1$, n_z can be allowed to take values larger than N, while maintaining $2n_\perp + |\Lambda| \leq N$. In fission, the nucleus elongates along the z axis, and the additional values of n_z introduced by a choice of $q > 1$ allow the use of a basis that is better adapted to the problem, without having to add additional (and largely irrelevant) values of the quantum numbers $n_\perp$ and Λ. Without the benefit of the parameter q, we would be forced to increase the maximum shell N in order to enlarge the basis, and the basis size (dropping a factor of two from the possible values of the spin-projection σ) would grow very quickly as

$$\dim \ = \ \frac{(N+1)\,(N+2)\,(N+3)}{6}$$

Through the use of the parameter q, relatively large values of n_z can be introduced, without significantly increasing the size of the basis. The final calculations presented in this report used $N = 13$, and $q = 1.5$, leading to values of n_z up to 19 and a basis size of dim = 763 (compared to dim = 1540 if we had taken $N = 19$ and $q = 1$, to achieve a similar range for $2n_\perp + \Lambda$ as well as n_z). The relatively large basis generated by the choice of $N = 13$, and $q = 1.5$ was required to describe the exotic shapes assumed by the nucleus on its way to scission (including the extreme configuration of two separated fragments). In addition to the

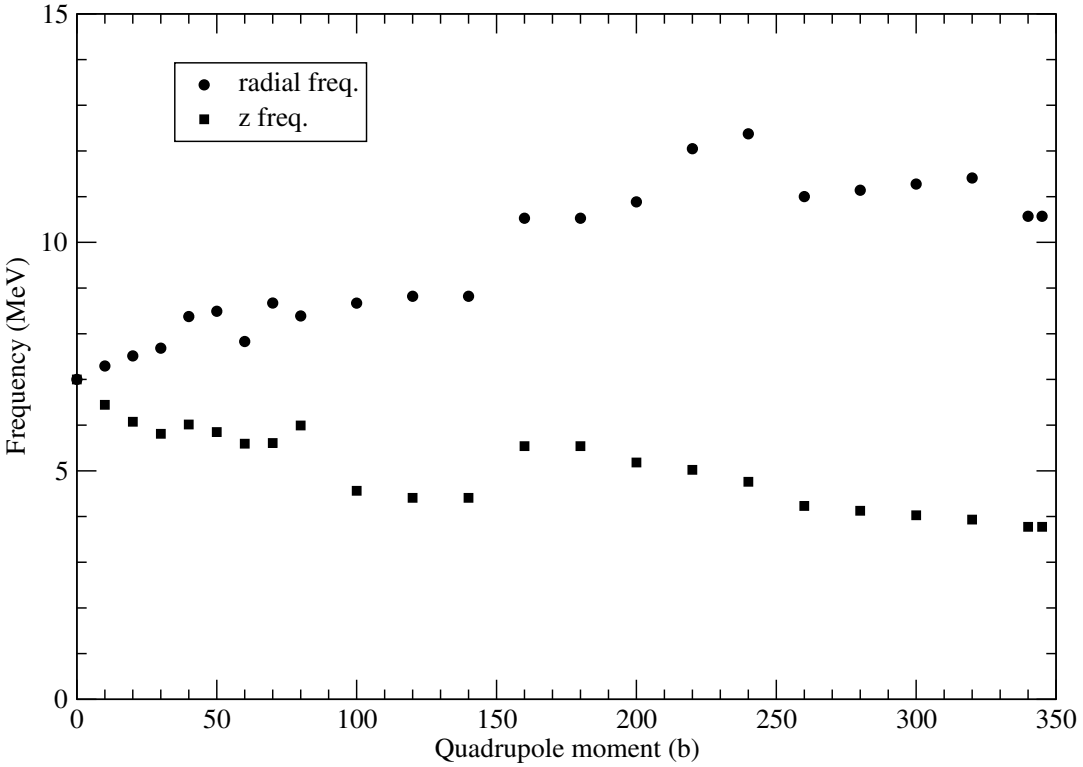

Figure 1: Plot of the harmonic-oscillator frequencies in the radial ($\hbar\omega_\perp$) and z ($\hbar\omega_z$) directions as a function of quadrupole moment, chosen to minimize the HFB energy.

choice of N and q, two frequencies, $\omega_\perp$ and ω_z, control the shape of the harmonic-oscillator functions. By adjusting these values, the basis functions can be optimally concentrated in the region that the nucleus occupies. In practice, these frequencies are varied to minimize the HFB energy. In the present calculations, this was done using $N = 12$ and $q = 1.5$ (for faster calculations), and the optimal frequencies were then used in the final calculations with $N = 13$ and $q = 1.5$. The optimal values found for these frequencies are plotted in Fig. 1 as a function of quadrupole moment. As the nucleus becomes more deformed, the ratio of radial frequency to the frequency along the z axis can be seen to increase, following the expected ratio of the major to minor axis "length" of the nuclear density.

The finite-range Gogny effective interaction was used in the calculations, with the D1S parameterization [6]. The interaction consists of two central Gaussian terms, a spin-orbit

term, a density-dependent term, and a Coulomb term. The center-of-mass motion contribution to the kinetic energy is fully subtracted in the code by including one-body, as well as two-body terms [5]. The code allows for the exact calculation of both direct and exchange parts of the Coulomb interaction however, in order to speed up the calculations, an option to calculate the exchange contribution in the Slater approximation [9] was used. For the density-dependent part of the interaction, 48-point Laguerre and Hermite quadratures were used for the integral in the radial and z directions, respectively. Only the central part of the interaction was included in the pairing field. The code allows for the inclusion of the Coulomb term in the pairing field as well, but the numerical stability of this contribution in the large basis used has not been fully tested, and was therefore omitted in the present calculations.

III. RESULTS

The HFB energies are plotted in Fig. 2 for a calculation along the most likely fission path in ^{240}Pu. The notable features in the plot are the ground state at $\langle Q_{20} \rangle \approx 30$ b, the first barrier near $\langle Q_{20} \rangle = 60$ b, the second minimum near $\langle Q_{20} \rangle = 80$ b, and the second barrier near $\langle Q_{20} \rangle = 140$ b. Note that the calculated energy for the ground state, $E_{\rm HFB}$ = -1804.639 MeV, reproduces the experimental binding energy of -1813.476 MeV to better than 0.5%. The calculated height of the first barrier, $E_A = 10.3$ MeV, is higher than the value of 6.0 MeV deduced from measured fission probabilities [10], however the breaking of axial symmetry and the zero-point-energy correction, which are known to lower this barrier by several MeVs, have not been included in the present calculation. The values of the octupole moment, $\langle Q_{30} \rangle$, which were automatically optimized by the HFB calculation to minimize the energy, are plotted in Fig. 3. The right-left reflection symmetry of the nucleus is spontaneously broken at $\langle Q_{20} \rangle = 100$ b, and the octupole moment increases monotonically up to 46.0 b$^{3/2}$ at the "hot" scission point (where $\langle Q_{20} \rangle = 345$ b). Likewise, the hexadecapole moment is also adjusted automatically by the HFB procedure, and is plotted as a function of quadrupole moment in Fig. 4. The moment $\langle Q_{40} \rangle$ increases up to 190 b^2 at $\langle Q_{20} \rangle = 345$ b.

For each HFB solution, we can also plot the corresponding total nuclear density. The nuclear density for the HFB calculations constrained in $\langle Q_{20} \rangle$ only is plotted in Figs. 5-7 in

cylindrical coordinates. The sequence of figures clearly show the neck between the nascent fragments thinning out. Structures can also be observed forming inside the fragments. In Fig. 7, corresponding to $\langle Q_{20} \rangle = 345$ b, the neck separating the two nascent fragments has almost disappeared. It is not possible to push the calculations much beyond this point with only $\langle Q_{20} \rangle$ constrained, as the nucleus is prone to scission spontaneously. In order to approach the scission configuration, all moments up to the hexadecapole have been constrained, and $\langle Q_{40} \rangle$ has been decreased in small steps from its value at $\langle Q_{20} \rangle = 345$ b (namely $\langle Q_{40} \rangle = 190$ b^2). The HFB energies associated with each value of $\langle Q_{40} \rangle$ are plotted in Fig. 8. This figure can be thought of as a slice taken out of Fig. 4 in [3] at $\langle Q_{20} \rangle = 345$ b. As $\langle Q_{40} \rangle$ decreases from 190 b^2, the energy remains relatively constant until $\langle Q_{40} \rangle = 183$ b^2 is reached. Below this value, the energy begins to drop precipitously. We identify the point at $\langle Q_{40} \rangle = 182$ b^2 as the scission configuration, the point at which the nucleus is committed to scission. Fig. 9 shows the nuclear density at $\langle Q_{40} \rangle = 183$ b^2, just before scission, while Fig. 10 shows the density at scission ($\langle Q_{40} \rangle = 182$ b^2). In these last two steps to scission, the remnants of the neck can be seen to disappear very quickly.

IV. PLANNED WORK

In the present work, we have shown that the HFB code we have developed can be used to drive a nucleus, ^{240}Pu in this case, to scission. Once the scission configuration has been identified, many nuclear properties of interest can be extracted directly from the HFB solution. For example, the spatial integral of the nuclear density for $z < 0$ and $z > 0$ separately will yield the number of nucleons in each fragment. Likewise, the separate integrals of the energy density give the HFB energies of the individual fragments, which can be compared to HFB calculations of their ground-state energies to get their excitation energies at scission. We note again the richness of the microscopic approach which yields not a single energy, but a distribution of excitation energies for a given mass split, corresponding to the full gamut of scission phenomena from "cold" to "hot". The kinetic energy of the fragments can be deduced from the separation distance between their centers of charge, by calculating their mutual Coulomb-repulsion energy.

Furthermore, the work described in this paper serves as a blueprint for a more comprehensive set of calculations of scission configurations. In addition, the choice and optimization of

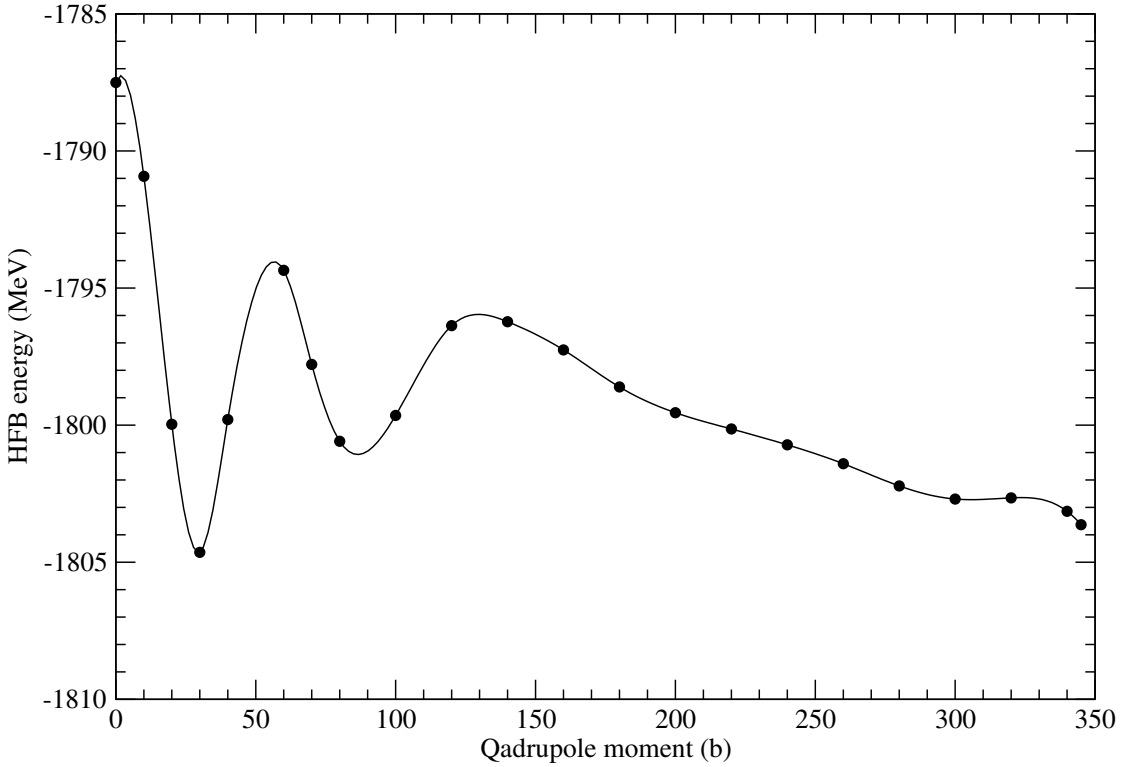

Figure 2: Calculated HFB energy as a function of quadrupole moment for ^{240}Pu. The calculation assumes axial symmetry, but reflection symmetry is spontaneously broken at a quadrupole moment value of 100 b. The solid points represent the actual calculated value, and a spline curve has been drawn through them to guide the eye.

the basis performed here can be used for further calculations in $(\langle Q_{20}\rangle, \langle Q_{30}\rangle, \langle Q_{40}\rangle)$, and the HFB solutions in the present work can serve as a starting point for those calculations. The procedure outlined here can be repeated to identify the "hot" scission configurations for a range of mass splits (i.e., constrained values of $\langle Q_{30}\rangle$). Then, for each exit point in the $\langle Q_{20}\rangle - \langle Q_{30}\rangle$ plane, $\langle Q_{40}\rangle$ can be constrained and gradually decreased to reach the scission configuration, as was done in Fig. 8. The same procedure can then be used to identify scission configurations at lower values of $\langle Q_{20}\rangle$ than that at which "hot" scission occurs, again by constraining $\langle Q_{40}\rangle$ and decreasing it until the neck separating the fragments breaks. To this end, a parallelized version of FRANCHBRIE has been written which assigns the calculation

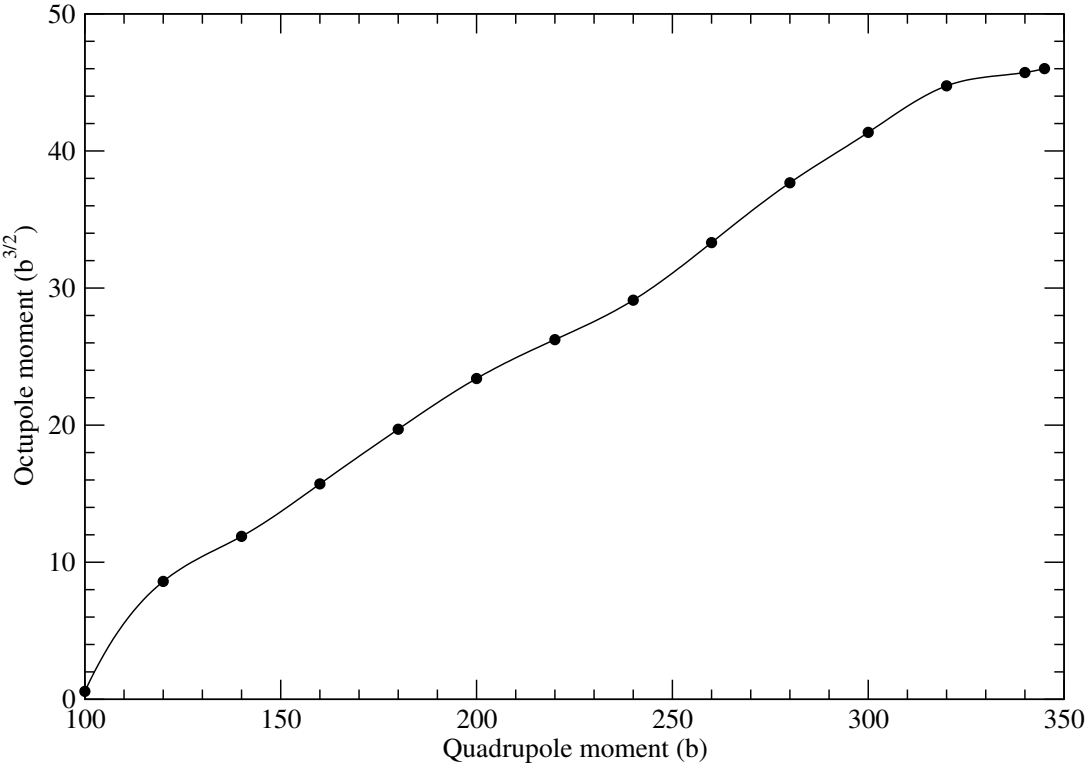

Figure 3: Plot of the octupole moment as a function of the quadrupole moment, corresponding to the calculation in Fig. 2.

for each set of constraints as a separate task to the first available cpu. This code will make it possible to search for a wide set of scission configurations in $(\langle Q_{20}\rangle, \langle Q_{30}\rangle, \langle Q_{40}\rangle)$ in a more efficient manner.

---

[1] O. Hahn and F. Strassmann, Naturwiss. **27**, 11 (1939).

[2] J. F. Berger, M.Girod, and D. Gogny, Nucl. Phys. **A428**, 23 (1984).

[3] J. F. Berger, M. Girod, and D. Gogny, Nucl. Phys. **A502**, 85 (1989).

[4] H. Goutte, J. F. Berger, P. Casoli, and D. Gogny, Phys. Rev. C **71**, 024316 (2005).

[5] W. Younes and D. Gogny, LLNL Tech. Rep. UCRL-TR-227645 (2007).

[6] D. Gogny, Proceedings of the International Conference on Nuclear Selfconsistent Fields, Tri-

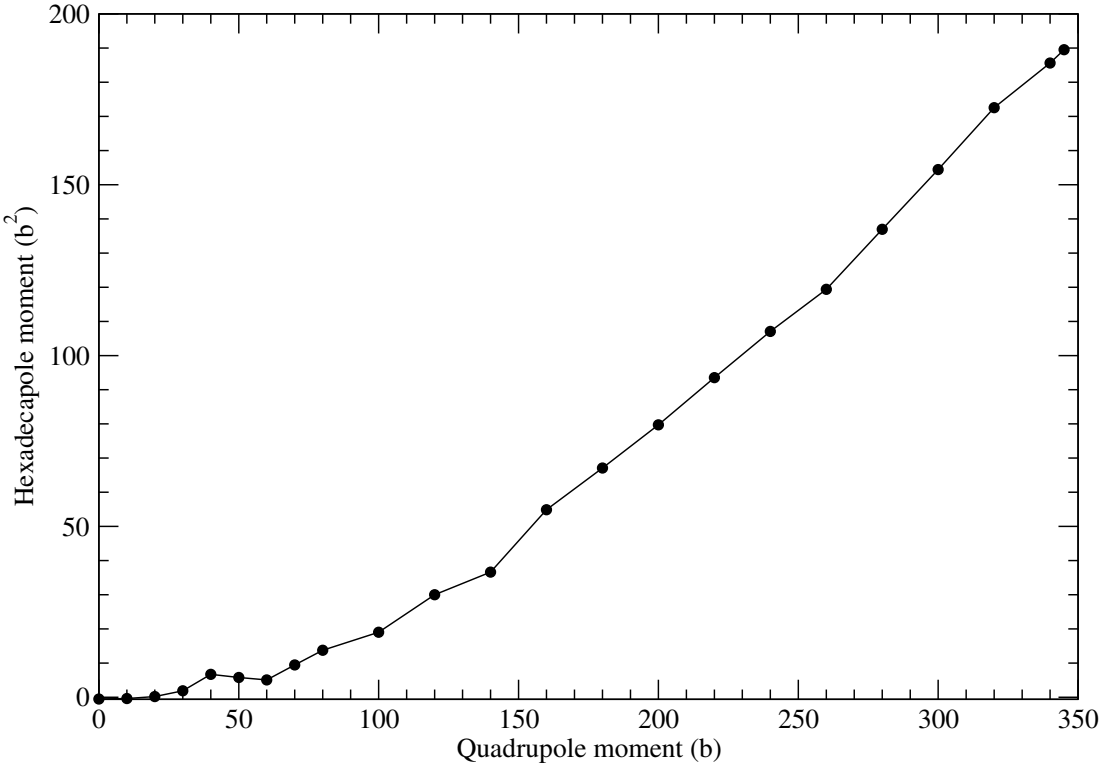

Figure 4: Plot of the hexadecapole moment as a function of the quadrupole moment, corresponding to the calculation in Fig. 2.

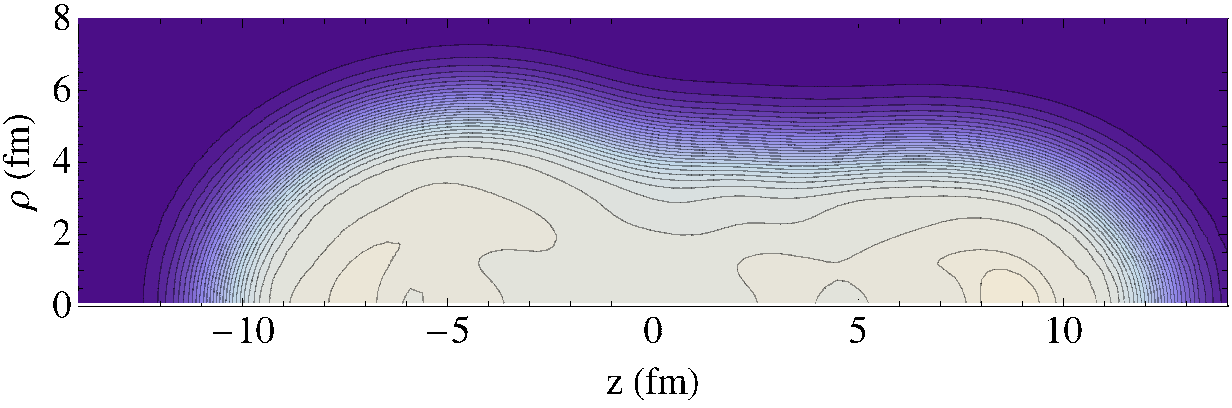

Figure 5: Contour plot in cylindrical coordinates of the total nuclear density calculated for ^{240}Pu at $\langle Q_{20} \rangle = 140$ b.

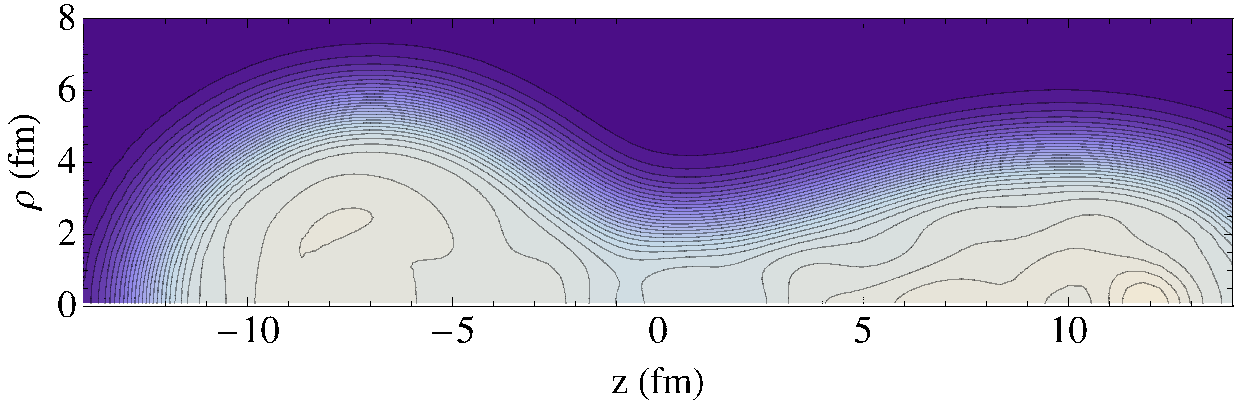

Figure 6: Contour plot in cylindrical coordinates of the total nuclear density calculated for ^{240}Pu at $\langle Q_{20} \rangle = 300$ b.

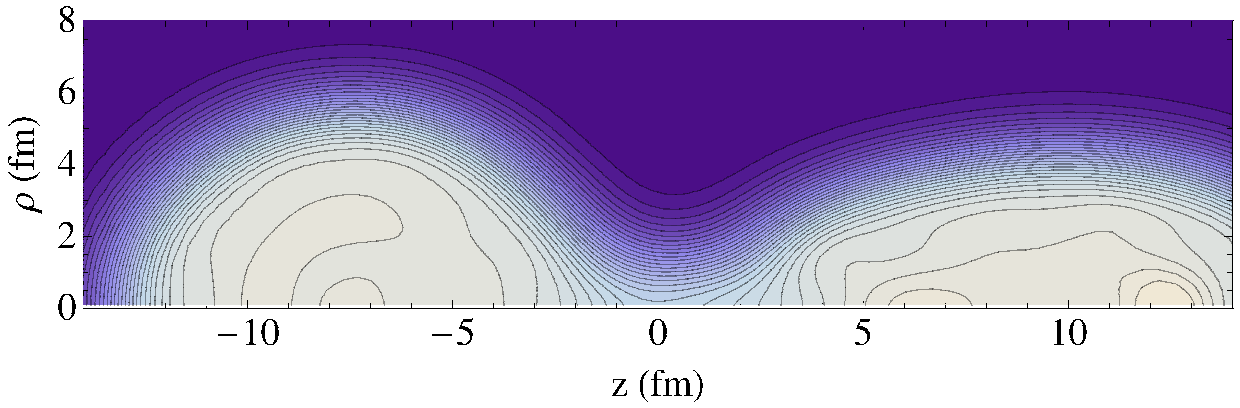

Figure 7: Contour plot in cylindrical coordinates of the total nuclear density calculated for ^{240}Pu at $\langle Q_{20} \rangle = 345$ b.

este, (1975).

[7] J. Decharge and D. Gogny, Phys. Rev. C **21**, 1568 (1980).

[8] N. N. Bogoliubov, Sov. Phys. JETP **7**, 41 (1958).

[9] J. C. Slater, Phys. Rev. **81**, 385 (1951).

[10] H. C. Britt, LANL report LA-4R-79-533 (1979).

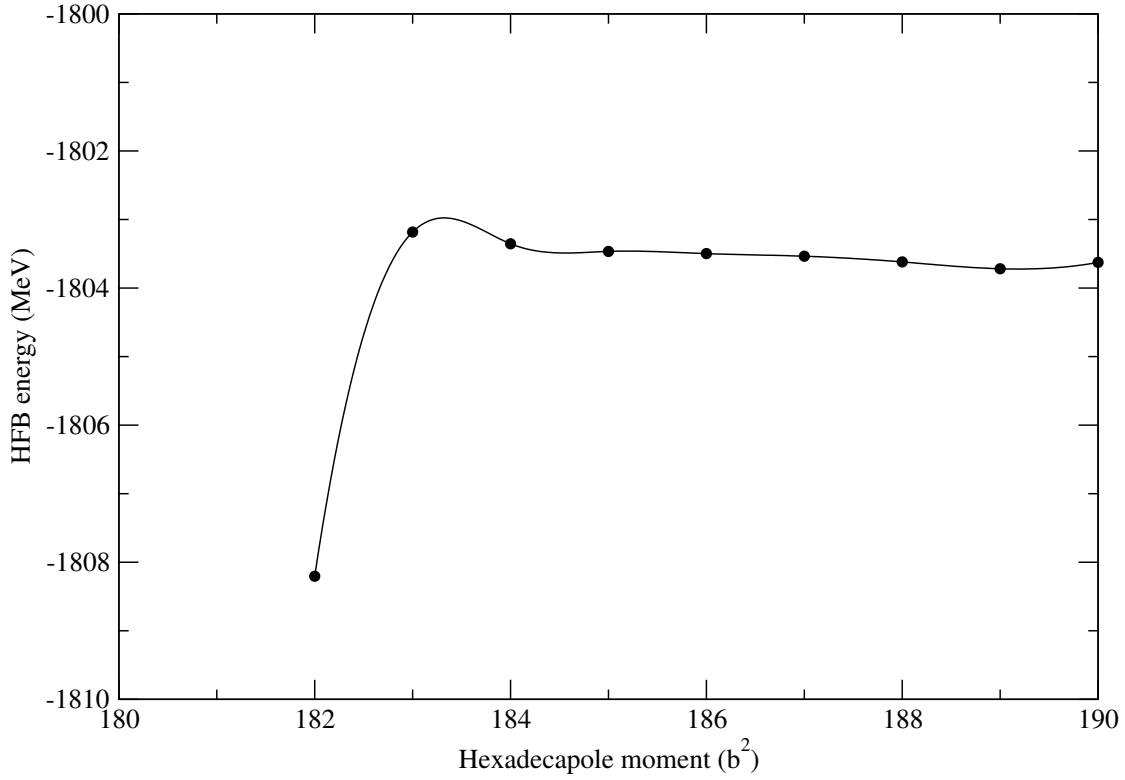

Figure 8: Plot of the HFB energy in ^{240}Pu as a function of hexadecapole moment, with all moments up to the hexadecapole constrained

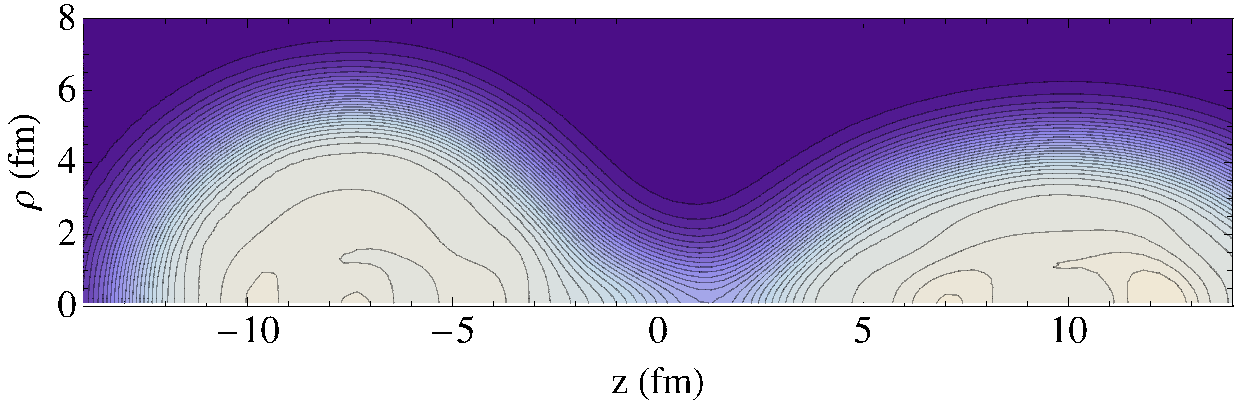

Figure 9: Contour plot in cylindrical coordinates of the total nuclear density calculated for ^{240}Pu at $\langle Q_{40} \rangle = 183$ b^2. All other moments have been constrained to their values for the calculation corresponding to Fig. 7.

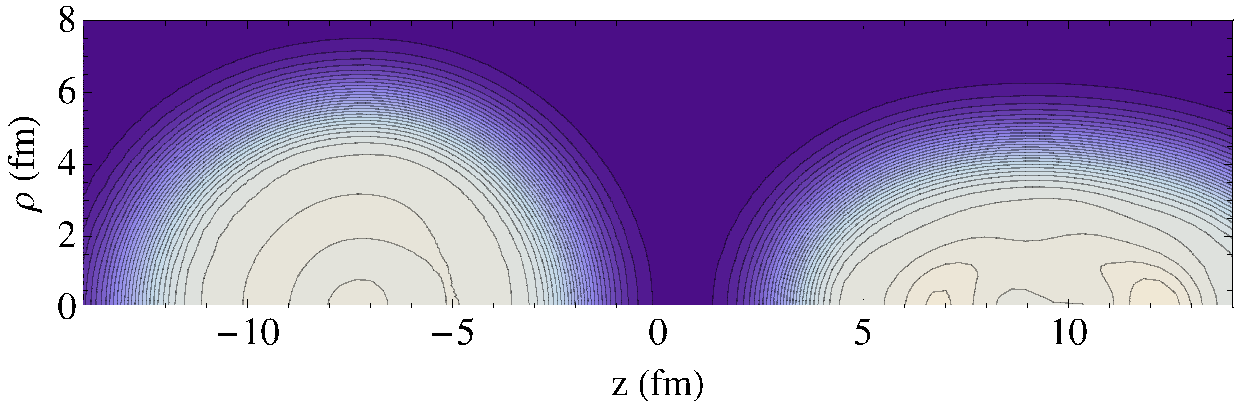

Figure 10: Contour plot in cylindrical coordinates of the total nuclear density calculated for ^{240}Pu at $\langle Q_{40} \rangle = 182$ b^2. All other moments have been constrained to their values for the calculation corresponding to Fig. 7.